

Preliminary Testing of a Coaxial Hall Thruster with a Diamond Nose Cone

IEPC-2005-191

Presented at the 29th International Electric Propulsion Conference, Princeton University,
October 31 – November 4, 2005

Nicolas Gascon^{*}, W. Scott Crawford[†], Ronald L. Corey[‡] and Mark A. Cappelli[§]
Stanford University, Stanford, CA, 94305, USA

and

David White^{**}
WE Research, LLC, Rosamond, CA 93560, USA

This paper describes our recent efforts in the integration of thick plate polycrystalline chemical vapor deposited (CVD) diamond into Stationary Plasma Thruster channel for improved wear resistance. Prior tests on laboratory Hall discharges indicated that CVD diamond has significant erosion resistance compared to the more commonly used boron nitride ceramics. Here, we extend our studies further, and have designed and have carried out preliminary tests of a diamond replacement nose cone on a commercial, space-qualified, BHT-200 low power Hall thruster. A preliminary performance test verified that the introduction of the diamond nose cone resulted in nearly identical levels of thrust, efficiency, and specific impulse, within experimental uncertainty. The operation on diamond resulted in a minor increase in current, most likely due to the rougher shape of the diamond test nose cone assembly, or of the use of an alumina fastener for mating the assembly to the central pole piece of the thruster. Future diamond assemblies will consist of diamond plates that are brazed together for improved mechanical and thermal performance. In parallel, we have developed and performed initial vibration testing of brazed diamond plates, to verify the mechanical integrity of the proposed (brazed) diamond nose cone assembly. Broadband sine-sweep testing at $1/3 g_{RMS}$ of two $6.1 \text{ mm} \times 5. \text{ mm} \times 1 \text{ mm}$ brazed diamond plates showed a nearly rigid frequency response over the range of 20 - 2000 Hz, with some resonances at higher frequencies, outside of the normal environmental testing range. Extended vibrations at 20 Hz, and at $3.7 g_{RMS}$ showed no noticeable shifts or degradation in the frequency response of the structure.

Nomenclature

BHT-200	=	Busek company's 200 W coaxial Hall Thruster
BN	=	Boron Nitride
CVD	=	Chemical Vapor Deposition
LHT	=	Stanford University's Linear Hall Thruster
m	=	mass of total nose cone (4.5 g) or test mass (5.1 g)
$a(t)$	=	instantaneous acceleration

^{*} Research Associate, Mechanical Engineering Department, Thermosciences Group, MC 3032.

[†] Research Assistant, Mechanical Engineering Department, Thermosciences Group, MC 3032.

[‡] Research Assistant, Mechanical Engineering Department, Thermosciences Group, MC 3032.

[§] Professor, Mechanical Engineering Department, Thermosciences Group, MC 3032.

^{**} Research Engineer.

h	=	distance from test layer to center of mass of m (6.8 mm for nose cone, 6.9 m for test)
r_2	=	outer diameter (6.53 mm)
r_1	=	inner diameter (4.79 mm)
l	=	length of rectangle (6.12 mm), parallel to direction of $a(t)$
w	=	width of rectangle (5.82 mm), normal to direction of $a(t)$
$F(t)$	=	instantaneous transverse shear force at cross section of interest
$M(t)$	=	instantaneous bending moment at cross section of interest

I. Introduction

HALL effect plasma thrusters¹ are now considered the propulsion of choice for several kinds of space missions, including station keeping, orbit raising, and interplanetary exploration. Being an electrostatic plasma accelerator, the Hall thruster offers high specific impulse (> 1500 s), moderate thrust (100 – 200 mN) and high efficiency (> 50 %) for input powers in the 1 – 10 kW range. Another interesting feature of the Hall thruster is the self-consistent accelerating electrostatic field, which results from the electron flow being retarded by a transverse magnetic field. This offers a clear advantage over the classical ion thruster configuration, where the accelerating grids are subject to intense erosion from ion bombardment, and impose a limitation on thrust density due to space charge buildup.

Following many years of research, development, and operation in ground facilities as well as in flight, the Hall thruster technology has attained a good level of maturity, which adds to its intrinsic advantages to make it a strong contender for future high power (several tens or even hundreds of kilowatts), deep-space missions. However, the duration of such missions will also exceed the demonstrated lifetime of any Hall thrusters that have been operated until now. It then becomes necessary to explore new ways of extending the Hall thruster lifetime, even if it means trading off some of its efficiency.

In a Hall thruster, the operational life is mainly limited by the erosion of the discharge chamber walls caused by the small fraction (< 10 %) of high-energy (several hundreds of electron-volts), heavy ions (usually xenon), which diverge from the bulk of the plasma beam. The rate of this sputtering is dependent on the type of material used for the discharge chamber. In the “magnetic layer” type Hall thruster, also called Stationary Plasma Thruster (SPT), the walls of the discharge chamber are electrically insulating, essentially for avoiding steep electron temperature gradients that could compromise the stability of the discharge. Modern SPTs have channel walls made of ceramics composed for a major part of Boron Nitride (BN), because of the associated low discharge current for a given thrust and specific impulse. Unfortunately, BN is also poorly resistant to ion bombardment, with sputter yields generally higher than those of other ceramics, such as alumina (Al_2O_3).

In order to study the effect of wall materials on Hall thruster operation and lifetime, we built a prototype SPT, which features a novel, linear geometry (*i.e.* with open electron drift), as opposed to the conventional annular discharge chamber (with closed electron drift). Using this Linear Hall Thruster (LHT), we showed that polycrystalline diamond could advantageously replace Boron Nitride as a channel wall material²⁻⁶, with erosion rates at least 3 times lower, and with lower discharge currents (keeping all other parameters the same). Although the thrust efficiency of the diamond lined LHT was not measured at the time, the propellant utilization was found to be comparable to that of the BN-lined discharge.

In this paper, we present the first effort to integrate polycrystalline diamond into the channel of a coaxial, flight qualified Stationary Plasma Thruster, the Busek BHT-200^{7,8}. A practical challenge is imposed by the fact that to our knowledge, CVD diamond can be made only in plate form, up to 1 mm thick, and the fabrication of monolithic pieces of cylindrical or more complicated shapes is not yet possible. We propose to match the shape of the original boron nitride nosecone by stacking along the same axis several planar rings and discs that will be brazed together and beveled to a near identical shape of the BN component. The aim of our study here is (i) to check, as suggested by our experience of the Stanford LHT, that replacing some of the BHT-200 boron nitride channel with polycrystalline diamond will not significantly degrade the overall performance of the thruster; and (ii) to evaluate if the proposed diamond nosecone design has strong chances of meeting space hardware qualification standards, in particular in terms of resistance to space launch vibrations. In the first section of this paper, we describe the operation of the BHT-200 with a nosecone made of diamond rings that are mechanically fastened together and to the thruster with a ceramic screw. The rings are neither brazed nor beveled at this point. In the second section, we experimentally assess the effect of low amplitude vibrations, within a frequency range typical of a space launch, on a sample brazed diamond assembly.

II. Thrust efficiency measurements

A. Thruster and diamond nosecone

The coaxial Hall thruster used in this study is Busek company's flight qualified BHT-200-X3⁷. The nominal operating conditions of this thruster are: anode xenon flow rate, 840 $\mu\text{g/s}$; cathode xenon flow rate, 98 $\mu\text{g/s}$; magnet current, 1.0 A; discharge voltage, 250 V; discharge current, 890 mA.

The center nosecone piece is schematically illustrated in Fig. 1. The tip of this nosecone (region colored in blue in Fig. 1) is the part of the thruster that erodes the most during operation, because of the intense ion bombardment that occurs there⁸. For the purpose of our tests, we have designed a diamond insulator assembly for replacing the original boron nitride tip. This assembly is composed of several, 1 mm thick planar rings made of CVD diamond. An alumina screw passing through the rings and into a tapped hole in the central pole piece holds the assembly together and onto the thruster (see Fig. 2, inset). Note that the tapped hole was not originally present in the thruster with a boron nitride tip, but it was verified with a finite element simulation that the impact on the thruster's applied magnetic field is negligible. Note also that the upstream part of the nosecone and the outer channel wall are still made of boron nitride.

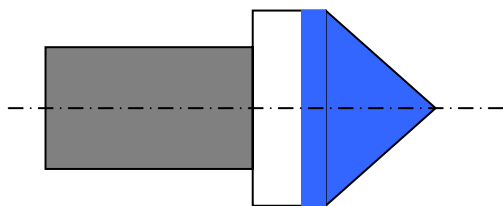


Figure 1. Schematic of the BHT-200 center boron nitride piece. The gray-colored region is not exposed to the plasma. The blue-colored region is replaced with CVD diamond rings and an alumina fastening screw.

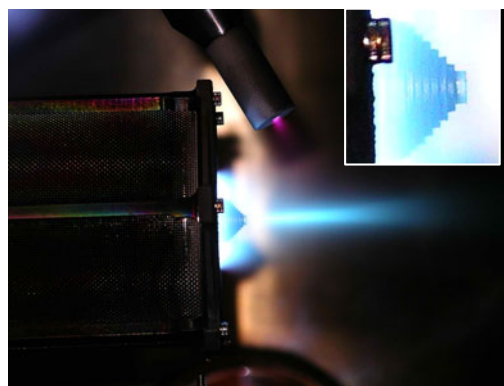


Figure 2. BHT-200 thruster with a diamond nosecone assembly running inside Stanford University's vacuum facility. Inset: details of the nosecone.

B. Vacuum facilities and diagnostics

The thrust efficiency measurements were performed at Stanford University's facility, which is a 3.25 m long nonmagnetic stainless steel vacuum chamber, 1.25 m in diameter. During nominal operation of the thruster, the pressure inside the chamber is kept to approximately 3×10^{-4} Pa (as measured using an ion gauge uncorrected for xenon) by a two-stage cryogenic pumping system (CVI, model number TM1200) cooled down by a helium refrigerator for the cryopanel and a flow of liquid nitrogen for the shroud. Separate DC power supplies are used for the discharge, cathode keeper, cathode heater, and electromagnets. The thruster is electrically isolated from the supporting structure. The macroscopic thruster parameters (discharge voltage, anode current, etc.) are monitored and recorded at a 1 Hz data rate with an Agilent data logging system.

Thrust is measured using an inverted pendulum type scale, which is represented schematically in Fig. 3. The lower portion of the inverted pendulum is fixed to the vacuum chamber. The thruster is mounted upon the upper pendulum portion, which is kept horizontal by using an inclinometer for monitoring and a remotely controlled lever for adjusting the thrust stand inclination. The two pendulum portions are connected by several flexures, a restoring spring, the calibration system, the propellant feed lines and the electrical power lines. An electromagnetic damper restrains oscillations that couple into the thrust stand from the test environment. The displacement of the inverted pendulum is converted into a proportional voltage signal by a linear variable differential transformer (LVDT) made by Macro Sensors (model PR 812). The LVDT output signal is monitored and sampled at a 10 Hz rate with the Agilent data logging system, and the traces are recorded on a personal computer for further analysis. The thrust stand is water cooled to minimize the signal drift due to uneven thermal expansion of the various structure parts when the discharge is running. Calibration of the thrust stand is performed using an electric motor and pulley

system. Weights are suspended from the pulley attached to the inverted pendulum. The electric motor lowers or raises several weights of known masses (within 10^{-4} relative uncertainty). The deflection of the inverted pendulum for known calibration weights yields a linear displacement versus calibration force curve. Multiple thrust measurements and calibrations in various pressure and thruster operating condition have demonstrated that the system is linear within 1% tolerance and capable of detecting horizontal forces as weak as 0.1 mN.

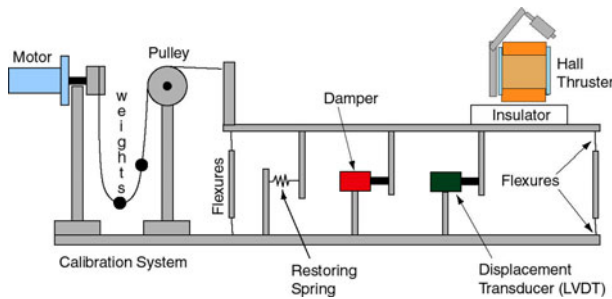


Figure 3. Stanford thrust stand schematic.

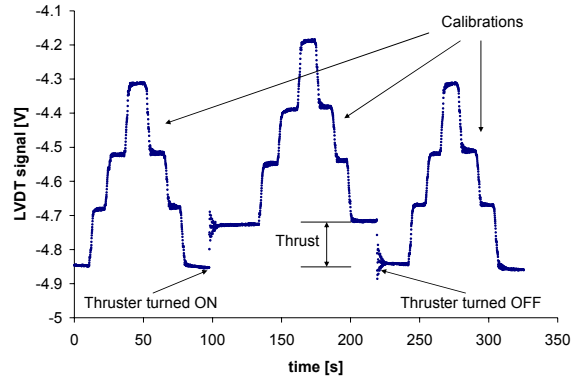


Figure 4. Sample LVDT signal trace recorded during thruster operation and thrust stand calibration.

For the thrust measurements presented hereafter, we systematically use 3 calibration weights. The thruster is warmed up at nominal operating conditions until no noticeable drift is observed in the discharge current and in the LVDT signal, then the discharge is turned off. Figure 4 describes what happens next. The reference signal (discharge off), the thrust signal (discharge on), and then the reference signal again are recorded for at least 10 s and calibrated. The whole procedure is repeated 5 times for every operating point. It should be noted that the xenon gas is always flowing through the anode and the cathode during the whole procedure. The extra force due to the cold gas expanding in vacuum is not taken into account in our measurements, but we verified that it amounts to only a few percent of the total thrust, at most.

C. Results

After a warming up period of approximately 15 minutes, the BHT-200 with a diamond nosecone was operated for one hour at nominal operating conditions. During the whole time, the thruster's behavior (visual aspect of the plume, discharge current stability, etc.) looked very similar to that of the original thruster. It was observed that the fastening screw turned red hot even at moderate discharge power, probably as a result of the intense flux of electrons caused by the tight convergence of the magnetic field lines at that location. In future tests, we will consider suppressing this hot spot by using a screw made of a material that conducts heat better than alumina. Molybdenum is our first choice, because of its high resistance to the sputtering caused by ion bombardment. The use of an electrical conductor in place of a ceramic may have additional impact on the discharge that would have to be evaluated.

Figure 5 shows the current-voltage characteristics of the BHT-200 for the original configuration and the diamond nosecone configuration. For these measurements, the discharge voltage was first set to 300 V, then decreased in 10 V steps until the discharge could no longer be sustained. With the diamond nosecone assembly this happened at a higher voltage (180 V) than with the reference thruster (80 V). Although this agrees qualitatively with prior results obtained with the Stanford LHT, it should be mentioned that the diamond

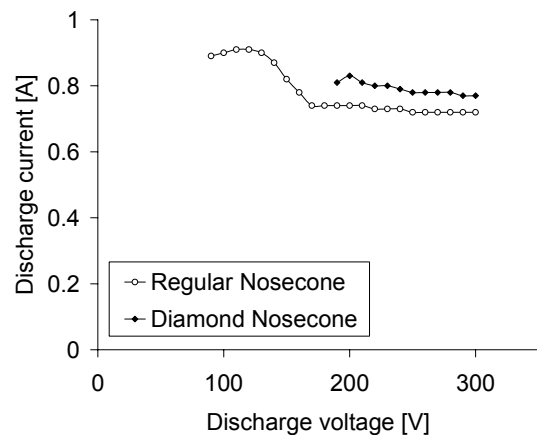


Figure 5. Busek's BHT-200 Current Voltage characteristics at Stanford University's facility.

thruster's current voltage characteristics were recorded after the reference case. Between the two series of measurements the thruster was operated several hours for other experiments, and during the diamond nosecone tests, the hollow cathode showed pronounced symptoms of aging (increased keeper voltage, difficulty to restart, etc.). It is then difficult to conclude that the higher thruster discharge shut down voltage is typical for the diamond nosecone configuration.

Between 200 – 300 V applied voltage, the discharge current is approximately 9 % higher with the diamond nosecone. This is probably not caused by the use of diamond, as the experiments performed with the LHT led to the contrary results. Two other effects may account for the supplemental discharge current. First, the staircase shape of the diamond assembly may increase the so-called near-wall conductivity of the electron flow across the magnetic field line. Previous experimental studies by Bugrova et al.⁹ indicated that the discharge current increases with the channel surface roughness, provided that the characteristic size of the surface irregularities is at least comparable to the electron Larmor radius. In our experiments, the second possible contribution to the extra discharge current is related to the presence of the fastening screw. Since alumina has a much higher secondary electron emission yield than boron nitride, near-wall conductivity at the tip of the nosecone is also increased¹⁰. To obtain a better quantitative assessment of those effects, future test plans include recessing the ceramic screw into the assembly and isolating it from the plasma with a brazed diamond disc, and also operating the thruster with a boron nitride nosecone that has the same staircase profile as the diamond stack.

Table 1. Thrust efficiency of the BHT-200.

Nose cone material	P_{back} , Pa	V_D , V	I_D , A	Power, W	Flow rate, mg/s	Thrust, mN	I_{sp} , s	η
BN	2.2×10^{-4}	200	0.72	144	0.85	8.72	1045	0.31
BN	2.3×10^{-4}	250	0.70	175	0.85	10.69	1282	0.38
BN	2.3×10^{-4}	300	0.70	210	0.85	12.15	1458	0.41
Diamond	2.2×10^{-4}	300	0.77	231	0.85	12.92	1549	0.43

The BHT-200 thrust efficiency measurements are summarized in Table 1. At 300 V applied voltage, operating the discharge in the diamond nosecone configuration resulted in more thrust, and in spite of the higher discharge current, thrust efficiency was also higher. It should be noted, however, that due to the hollow cathode problems mentioned above, we were able to record only one thrust trace during the diamond nosecone test, as opposed to five traces in the reference case. Moreover, the discharge was also less stable than usual at the time of thrust measurement, resulting in a wider spread of the signal. Nevertheless, within experimental uncertainties, thrust and efficiency of the BHT-200 with a diamond nosecone are nearly equal to those of the original thruster.

III. Testing the diamond braze

A. Presentation

In order to address the question of reliability of brazed diamond layers under vibratory loading such as that encountered in a space mission, a preliminary program of vibration testing was undertaken. In keeping with a NASA environmental testing standard¹¹, this program consisted of two components: sine sweep testing for resonant modes, and high-acceleration testing against failure. The test specimen available for this program was a brazed pair of diamond layers with the same thickness but a different shape than the actual nose cone. While the layers of the nose cone are circular rings or disks, the layers of the test specimen were rectangular. Analysis was required to establish conditions of similarity between the two shapes. A test apparatus was designed and built for flexible testing of these small parts, and the preliminary results are presented below.

B. Similarity Analysis

It was assumed that the braze layer of the nose cone most susceptible to vibratory failure is the base layer, since it has the greatest seismic mass suspended from it. This braze layer connects two diamond rings of outer diameter 13.06 mm and inner diameter 9.58 mm. The braze layer of the test specimen, on the other hand, is a rectangle of dimensions

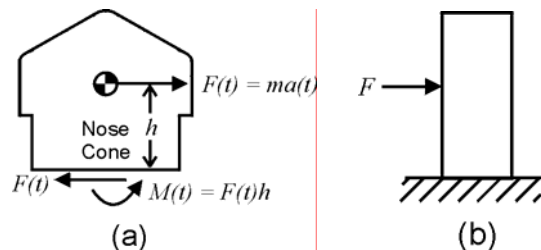


Figure 6. Physical models for braze testing.
(a) Quasi static inertial force on nose cone.
(b) Beam analogy.

6.12 mm × 5.82 mm. The following analysis was used to establish conditions of similarity in the stress applied to these braze layers under vibratory loading. A static stress analysis was used to approximate the dynamic similarity conditions for off-resonant frequencies, understanding that resonant frequencies are not likely to be the same for the two different geometries. That is, for the purposes of similarity alone, the assembly was considered to act as a perfectly rigid body at environmental testing frequencies. This approximation was tested by experimental modal analysis, as discussed below. The vibratory load in the case of the real nose cone was modeled as a quasi-static inertial force, $F(t) = ma(t)$, applied through the center of mass of diamond section of the nose cone (Fig. 6a). The quasi-static approximation assumed force and moment equilibrium as shown.

Table 2. Static stress formulae for point-loaded, cantilevered beams of relevant cross-sectional shapes.

Cross-section	Maximum normal stress in cross section	Maximum shear stress in cross section
Hollow circle (actual nose cone)	$\sigma_{\max}^{\text{circle}}(t) = \frac{4ma(t)hr_2}{\pi(r_2^4 - r_1^4)}$	$\tau_{\max}^{\text{circle}}(t) = \frac{4ma(t)(r_1^2 + r_1r_2 + r_2^2)}{3\pi(r_2^4 - r_1^4)}$
Rectangle (test piece)	$\sigma_{\max}^{\text{rectangle}}(t) = \frac{6ma(t)h}{lw^2}$	$\tau_{\max}^{\text{rectangle}}(t) = \frac{3ma(t)}{2lw}$

Figure 6a presents a loading similar to that of a cantilevered beam with point-force applied (Fig. 6b), so a beam analysis was applied to estimate stresses in the plane of the base braze attachment. The analysis was carried out for a beam of hollow circular cross-section for the case of the actual nose cone, and for a rectangular cross-section for the case of the test piece. According to Ref. 12, the maximum normal and shear stresses occurring are given by Table 2.

Figure 7 schematically shows the test piece itself. The test mass, which was bonded to the brazed pair of rectangular diamond layers, included an accelerometer for modal testing. It was designed for one-dimensional vibration in the direction shown, and the test mass was balanced about the centerline of the upright aluminum strut. The diamond layers had a smooth and a rough side, and bonding agents were chosen differently for each. For the smooth side, ethyl cyanoacrylate glue (Instant Krazy Glue) was used, while a high strength two-part epoxy (3M Type 2216) was used on the rough side. These bonded joints were statically tested to have ample strength prior to vibratory testing.

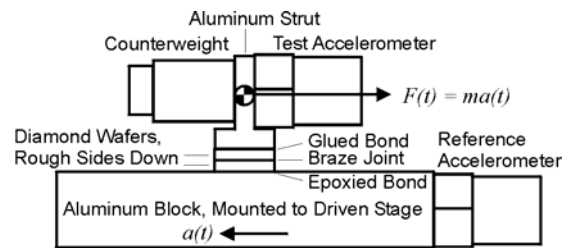


Figure 7. Brazed pair of rectangular diamond layers and attached test mass with accelerometers.

NASA GEVS documentation¹¹ was used to establish environmental test conditions. It specifies generalized test levels for STS or ELV launched components, in the form of acceleration spectral densities in the bandwidth 20 Hz – 2000 Hz. Components of mass less than 22.7 kg receive the full test levels, while more massive components may be tested at derated levels. The full qualification test level yields an overall RMS acceleration of 14.1 g_{RMS} (138 m/s^2). The equations in Table 2 were used to estimate the appropriate scaling factors to predict the test RMS acceleration required to achieve stresses in the test piece equivalent to those achieved in the real nose cone at 14.1 g_{RMS} .

Figure 8 presents these predicted stresses in the test piece and in the nose cone as a function of acceleration. The dotted lines indicate conversion from the stresses in the nose cone at 14.1 g to the condition of equivalent predicted maximum stress in the test piece. Depending on whether one matches normal stress or shear stress, the equivalent value of acceleration in the test piece is predicted to be either 3.1 g or 9.4 g. We chose to use the normal-stress scaling for this

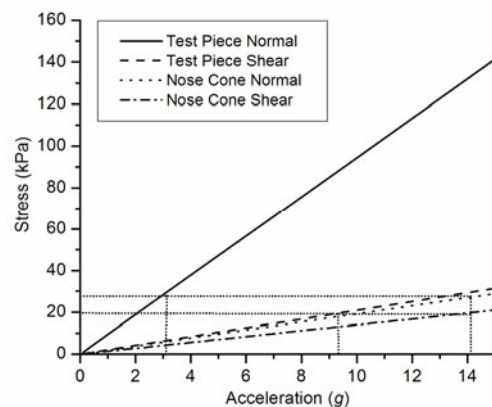


Figure 8. Predicted Stresses in Nose Cone and in Test Piece

study, so test acceleration of at least $3.1 g_{RMS}$ was chosen. Achieving $9.4 g_{RMS}$ requires a minor change to the facility and will be tested in the near future.

C. Test Apparatus

Figure 9 illustrates the vibration testing system. The test apparatus consisted of the following components, in addition to the test assembly shown in Fig. 7. The mini-vibration-table consisted of a small aluminum plate on a linear bearing. It was driven by a voice coil actuator (H2W Technologies NCC05-18-060-2X), using a wideband high current audio amplifier (McIntosh MC2100) as its power source and a programmable function generator (Stanford Research Systems DS345) as its signal source. Compression springs were used to improve the sinusoidal response of the table by reducing overshoot. The key sensors in the measurement were the two piezoelectric accelerometers shown in Fig. 7 (Bruel & Kjaer 4393), whose signals were conditioned with a charge amplifier (Bruel & Kjaer 2635). Data from these sensors and from the excitation signal were acquired by one of two instruments, depending on the frequency range of the measurement. For frequencies up to 20 kHz, a PC with National Instruments LabView software was used with a data acquisition card (Keithley KPCI-3108). For frequencies above 20 kHz, a digital oscilloscope was used (Tektronix TDS3014). Data were then processed using the Fast Fourier Transform (FFT) functions in Microcal Origin software. During an acquisition of data, a single pass sweep was recorded. Therefore a rectangular FFT window was used, in order not to diminish the signal at each end of the sweep. The FFT leakage that may have ensued should be negligible, at least for the frequencies up to 20 kHz, because of the high frequency resolution obtained by the long sample periods used.

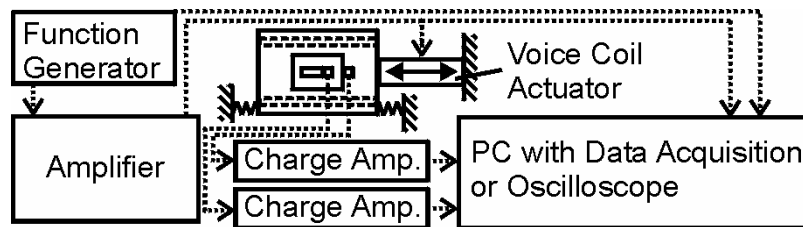


Figure 9. Schematic of vibration test facility, shake table shown in top view.

D. Methods and Results

The test procedure included two phases. First, modal testing was done to identify resonant frequencies within the test assembly. This was done by sine sweep testing at approximately $1/3 g_{RMS}$, first over the qualification test bandwidth of 20 Hz – 2 kHz, then over an extended bandwidth of 2 kHz – 65 kHz. The extended bandwidth was tested to identify resonant frequencies that may be associated with the braze joint. With the future addition of analytical or experimental modeling for assignment of such frequencies to the brazed structure, detecting shifts in these frequencies may be a viable nondestructive test for microscale damage in the braze joint.

The modal test was conducted by successive sine sweeps in subsets of the total frequency bandwidth, FFT conversion of each accelerometer's response into power spectral densities, combining these data into an amplitude frequency response function (FRF), and plotting the full spectrum of FRF by composing the sub-bands onto a single graph. For each sub-band, the function generator was programmed to perform a linear, single pass sweep through the band, with amplifier gain adjusted to keep the reference accelerometer's RMS output approximately constant near $1/3 g_{RMS}$. Parameters of the sweep, data acquisition, and low-pass filtering of the analog signal were chosen to accomplish high resolution of frequency resolution in the FFT while avoiding problems of leakage or aliasing¹³. For example, the first sub-band was swept from 15 Hz to 50 Hz over an 82 second sampling period, taking 65536 samples at a rate of 800 Hz for a Nyquist frequency of 400 Hz and frequency resolution 0.012 Hz, with the low-pass filter attenuating at -24 dB by 800 Hz. The high frequency scans were limited to 10,000 point samples due to the storage limits of the oscilloscope, so their frequency resolution is more limited.

The quantity plotted in the modal testing results is the modulus of the complex amplitude frequency response function (FRF), which is simply calculated at each frequency as the ratio of the modulus of the FFT of the measured test acceleration to that of the measured reference acceleration¹³. The case $|FRF|=1$ at a given frequency represents rigid behavior of the structure connecting the reference and test accelerometers at that frequency. Peaks in $|FRF|$ are likely to represent resonant frequencies of the structure connecting the two accelerometers, while valleys in $|FRF|$ represent damping. It should be pointed out that the test assembly includes elements of likely lesser stiffness than the

braze joint, namely the epoxied and glued joints and the aluminum strut. The epoxy and glue are also likely to have damping characteristics at some frequencies. Thus it is likely that many of the peaks and valleys in the modal plots are not associated with the braze joint. Further work would be required to assign any spectral feature to the braze joint.

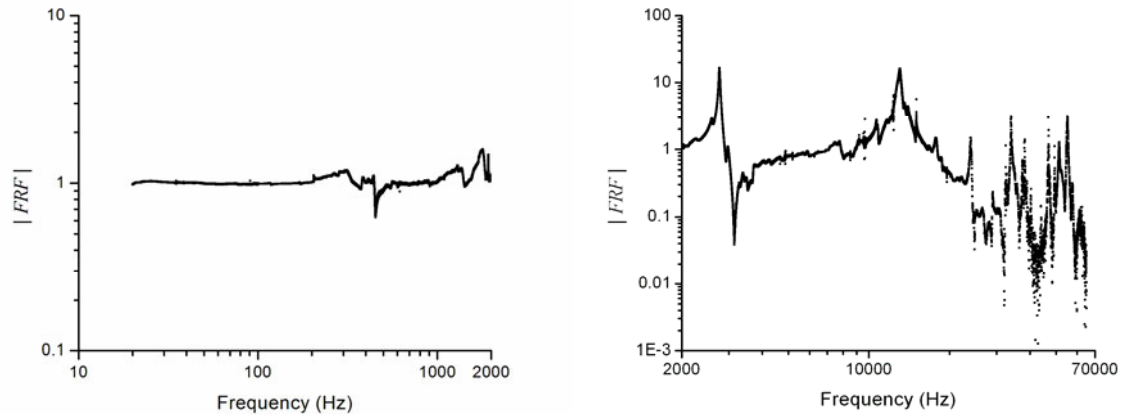


Figure 10. Modal Testing Results Prior to Higher Acceleration Testing.

The results of the modal testing are shown in Fig. 10. In the band of random vibration testing from Ref. 13 (20 Hz – 2 kHz, left pane of Fig. 10), there are no significant peaks. At higher frequencies (Fig. 10., right pane), significant peaks can be found at 2768 Hz, 13079 Hz, 34012 Hz, and 55252 Hz.

Since no significant peaks were found in the 20 Hz – 2 kHz band, and because the facility is not currently programmable for random vibration testing, the generalized random vibration test was simulated with a single-frequency test at the same overall RMS acceleration level. The table was driven at 20 Hz, $3.7 g_{RMS}$, for a total of 3.5 minutes. The GEVS specification requires 1 minute each along three axes, but this test was conducted just along one axis. Data were taken at the beginning and at the 3 minute mark of the test (16384 samples at 1024 Hz sampling rate, low-pass filtered to –24 dB by 400 Hz). Four observations were made in order to detect any damage that may have occurred. First, a visual inspection of the assembly revealed no sign of damage. Second, the real-time data of the 20 Hz traces from the beginning and end of the test were compared for any change in the absolute or relative response of the two accelerometers. Again, no change was visible. Third, the accelerometer traces were processed by FFT, and the phase angle difference between the reference and test accelerations at 20 Hz was compared. The difference prior to the test was 2.78° , and after the test it was 2.76° . These values are identical to within the experimental uncertainty. Fourth, the 2 kHz – 65 kHz band was swept again (Fig. 11) and the FRF spectrum compared with that before the test (Fig. 10). The spectra are very similar, with the locations of the prominent peaks mentioned above having shifted by only 0.04 % – 0.6 % (2787 Hz, 13143 Hz, 34027 Hz, and 55008 Hz, respectively). These shifts are likely to be within the experimental uncertainty. As discussed above, all features of the spectrum remain unassigned to structural components at this time, so they are shown here only as an item of preliminary interest for possible future study.

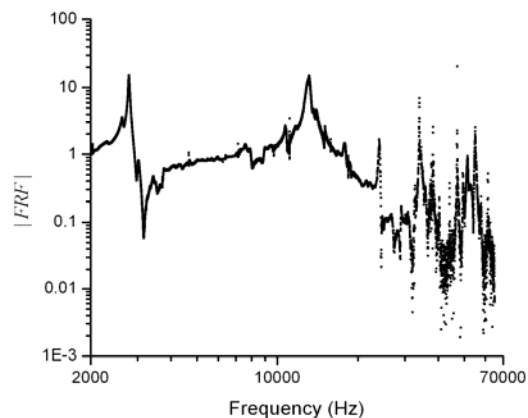


Figure 11. Modal Testing Results After Higher Acceleration Testing.

IV. Summary and Future Work

This paper presented our continuing effort to increase Stationary Plasma Thruster lifetime by replacing the parts of the boron nitride channel walls, which erode the fastest under ion bombardment, with an insulator made of polycrystalline chemically vapor deposited diamond.

A first test consisted in replacing the nosecone tip of a flight-qualified, 200 W coaxial SPT with an assembly made of CVD diamond rings shaped to the design of the original nosecone, and fastened to the central pole piece with an alumina screw. Preliminary results indicate that the operation of the SPT at nominal conditions and its thrust and thrust efficiency are nearly unaffected by the use of the diamond nosecone, within experimental uncertainty. Future diamond assemblies will consist of diamond plates that are brazed together for improved mechanical and thermal performance. In parallel, we have developed and performed initial vibration testing of brazed diamond plates, to verify the mechanical integrity of the proposed (brazed) diamond nose cone assembly. Within the limitations of this study, the brazed diamond has performed well under vibratory loading. These limitations include the use of a quasi-static approximation for scaling dynamic stresses from the real nose cone to the test piece, the choice thus far to test only to the lower scale level of acceleration, and the several methods of damage detection mentioned above. The test piece will be further tested at higher levels of acceleration, and the real brazed diamond nose cone will be tested.

Acknowledgments

This work is funded in part by the Air Force Office of Scientific Research. The authors would like to thank W. Hargus (Air Force Research Laboratory), V. Hrubby, B. Pote and R. Tedrake (Busek, Inc.) for providing the BHT-200 used in these tests, and for many comments and advice on its technology and operation. Our thanks also to J. Zimmer and J. Herlinger (*sp*³, Inc.) for providing the polycrystalline diamond samples used in this study, and to C. McLean (Pratt and Whitney) for his original assistance with the configuration of the thrust stand.

References

- ¹Zhurin V. V., and Kaufman H. R., "Physics of Closed Drift Thrusters" *Plasma Sources Sci. Technology* **8**, pp. R1-R20, 1999.
- ²Hargus W. A., Jr, and Cappelli M. A., "Development of a Linear Hall Thruster", *34th Joint Propulsion Conference, Cleveland, OH*. American Institute of Aeronautics and Astronautics, Washington, DC, 1998. AIAA-98-3336.
- ³Schmidt D. P., Meezan N.B., Hargus W.A., Jr., and Cappelli M.A., "A Low-Power, Linear-Geometry Hall Plasma Source with an Open Electron-Drift," *Plasma Sources Science and Technology* **9**, pp. 68-76, 2000.
- ⁴Cappelli M.A., Walker Q.E., Meezan N.B., and Hargus W.A., Jr., "Performance of a Linear Hall Discharge with an Open Electron Drift", *37th Joint Propulsion Conference, Salt Lake City, UT*, American Institute of Aeronautics and Astronautics, 2001. AIAA-2001-3503.
- ⁵Meezan N. B., Gascon N., and Cappelli M. A., "Linear Geometry Hall Thruster with Boron Nitride and Diamond Walls", *27th International Electric Propulsion Conference, Pasadena, CA*. Electric Rocket Propulsion Society, 2001. IEPC-01-39.
- ⁶Gascon, N., Thomas, W. A., Hermann, W. A., and Cappelli M. A., "Operating regimes of a linear SPT with low secondary electron-induced wall conductivity", *39th AIAA/ASEE/ASME Joint Propulsion Conference, Huntsville, Alabama*. American Institute of Aeronautics and Astronautics, Washington, DC, 2003. AIAA-2003-5156.
- ⁷Hargus W. A., Jr., and Reed G., "The Air Force Clustered Hall Thruster Program," *38th Joint Propulsion Conference, Indianapolis, Indiana*, American Institute of Aeronautics and Astronautics, Washington, DC, 2002, AIAA-2002-3678.
- ⁸Hargus W. A., Jr, and Charles C., "Near Exit Plane Velocity Field of a 200 W Hall Thruster", *39th AIAA/ASEE/ASME Joint Propulsion Conference, Huntsville, Alabama*. American Institute of Aeronautics and Astronautics, Washington, DC, 2003. AIAA-2003-5154
- ⁹Bugrova A. I., Morozov A. I., and Kharchevnikov V. K., "Experimental investigation of near wall conductivity", *Sov. J. Plasma Phys.* Vol. 16, No. 12, Dec. 1990, p 849
- ¹⁰Barral, S., Makowski, K., Peradzynski, Z., Gascon, N., and Dudeck, M., "Wall Material Effects in Stationary Plasma Thrusters II: Near-Wall and Inner-Wall Conductivity," *Physics of Plasmas*, Vol. 10, No. 10, Oct. 2003, p. 4137.
- ¹¹Milne, J.S., Garvin, J., Baumann, R., "General Environmental Verification Specification for STS & ELV Payloads, Subsystems, and Components," NASA GEVS-SE Rev A, 1996.
- ¹²Gere, J. M., and Timoshenko, S.P., *Mechanics of Materials*, 2nd ed., PWS-Kent Publishing Company, Boston, 1984, Chapter 5.
- ¹³Harris, C.M. (ed.), *Shock and Vibration Handbook*, 3rd ed., McGraw-Hill, New York, 1988, Chapter 27.